Chinese Chemical Letters 37 (2026) 112443

Contents lists available at ScienceDirect

Chinese Chemical Letters

journal homepage: www.elsevier.com/locate/cclet

Revealing the unique generation pathway of singlet oxygen from sulfate radical in Fe-based Fenton-like system

Taozhen Li[a,b], Zhuohang Wu[a], Shu Yang[a,*], Bin Li[c,f], Semencha Alexander Vyacheslavovich[d], Donaev Sardor Burkhanovich[e], Ergashev Yorqinjon Tolqinogli[e], Rashidov Shokhzodbek Abduvakhobovich[e], Lei Wang[a], Jingwen Pan[a,*]

[a] Key Laboratory of Eco-chemical Engineering, College of Environment and Safety Engineering, Qingdao University of Science and Technology, Qingdao 266042, China
[b] College of Environmental Science and Engineering, Ocean University of China, Qingdao 266100, China
[c] College of Materials Science and Engineering, Qingdao University of Science and Technology, Qingdao 266042, China
[d] Peter the Great St. Petersburg Polytechnic University, St. Petersburg 195251, Russia
[e] Tashkent State Technical University, Tashkent 100095, Uzbekistan
[f] Qingdao Key Laboratory of Inorganic Silicide Functional Molecular Synthesis, Qingdao Meigao Group Co., Ltd., Qingdao 266108, China

ARTICLE INFO

Article history:
Received 24 September 2025
Revised 3 December 2025
Accepted 21 January 2026
Available online 22 January 2026

Keywords:
Peroxydisulfate
Fe-based catalyst
Mo doping
Sulfate radical
Singlet oxygen

ABSTRACT

The effective Fe^{II}/Fe^{III} cycling and rapid activation of oxidants are the key problems that expand the application of iron-based Fenton-like reaction in water purification. Herein, bamboo-like Fe-Mo bimetallic catalysts (FeMo@CNT) were prepared to activate peroxydisulfate (PDS) for organic pollutants removal. FeMo@CNT/PDS system can completely degrade bisphenol (BPA) within 30 min ($k_{obs} = 0.444\ min^{-1}$, which was 17.1 times that of Fe@CNT/PDS system). Results showed that singlet oxygen ($^1O_2$) and sulfate radical ($SO_4^{\bullet-}$) were dominant reactive oxygen species in FeMo@CNT/PDS/BPA system, where $^1O_2$ was derived from superoxide radical ($O_2^{\bullet-}$) oxidized by $SO_4^{\bullet-}$. Mo species in FeMo@CNT/PDS system could accelerate the O–O breaking in PDS and reduce the energy barrier of $^1O_2$ production, thus achieving the increase of both $SO_4^{\bullet-}$ and $^1O_2$. Meanwhile, FeMo@CNT/PDS system exhibited good catalytic activity with wide pH and multiple environmental substrates. The high oxidation performance after 23 h in dynamic experiments further demonstrated the stability of this system. And the toxicity of the original pollutants was further declined, indicating that the FeMo@CNT/PDS system was ecologically friendly. This work provides new insights for solving hindered Fe^{II}/Fe^{III} cycle and proves a new mechanism of $^1O_2$ generation in SR-AOPs.

© 2026 Published by Elsevier B.V. on behalf of Chinese Chemical Society and Institute of Materia Medica, Chinese Academy of Medical Sciences.

Bisphenol A (BPA) is broadly utilized as additive in many industries, such as the production of food, toys, and plastic-related consumer goods [1]. Meanwhile, however, the risk of environmental exposure of the novel pollutant BPA is also increasing in aquatic environments. BPA have a serious impact on the endocrine system of human and animal body [2]. Therefore, it is urgent to study the cost-effective degradation strategies for BPA to address this situation. Sulfate radical ($SO_4^{\bullet-}$)-based advanced oxidation processes (SR-AOPs) have the advantages of high activity, good tolerance and easy storage, which received wide attention in water environment restoration [3–5]. Among them, persulfate (PS) activation is the key in SR-AOPs and the efficient, energy-saving and environmentally friendly transition metal heterogeneous activation strategy is a good choice [6]. Cheap, accessible and abundant transition metal Fe is a good raw material for catalyst synthesis [7]. Abundant Fe sites are conducive to PS activation and organic pollutants degradation [8]. However, the use of Fe-based catalysts in SR-AOPs is limited due to hindered Fe(III)/Fe(II) circulation [9].

Metal doping is a feasible and efficient strategy to enhance the activity of Fe-based catalysts [10]. Among them, the transition metal Mo, equipped with multiple valence states, has a strong interaction with Fe, which can stimulate the Fe redox reaction and enhance the Fe-based catalyst activity by the efficient electron transfer mechanism [11,12]. More and more research focus on the study of Fe/Mo-based catalysts. However, attention should be paid to the secondary contamination caused by the metal ion overflow

* Corresponding authors.
E-mail addresses: ys131350@163.com (S. Yang), jwpan@qust.edu.cn (J. Pan).

https://doi.org/10.1016/j.cclet.2026.112443
1001-8417/© 2026 Published by Elsevier B.V. on behalf of Chinese Chemical Society and Institute of Materia Medica, Chinese Academy of Medical Sciences.

from the catalysts. How to heighten the catalytic activity and stabilization of Fe/Mo-based materials is a noteworthy concern. Carbon materials are promising nonmetallic catalysts with large specific area and good electron transfer, but with relatively low catalytic activity [13,14]. The doping of heteroatoms into the carbon material is reported to produce holes or excess electrons, creating new active sites, which can enhance the catalytic activity of carbon material [15]. At the same time, combining transition metal with the carbon material can further fix the metal atoms and heighten the catalytic activity and stability [16–18]. Therefore, for actual application of Fe/Mo-based materials in SR-AOPs, it is a feasible strategy to fix Fe and Mo on a carbon matrix.

SR-AOPs mediated by Fe-based catalysts include radical-dominated mechanism and non-radical-dominated mechanism [19]. Radical-dominated AOPs can achieve high removal to organic pollutants in a short time, but often have weak resistance to environmental interference [20]. Non-radical-dominated AOPs with the advantages of strong resistance to environmental interference and good selective oxidation, are more suitable for wastewater treatment in complex environment [21]. Non-radicals, such as $^1O_2$, high-priced metals and electron transfer, will react preferentially with pollutants containing electron groups, thus improving the degradation of electron-rich pollutants such as BPA [21,22]. $^1O_2$ is an important ROS with oxidation capacity, which could frequently detected in the field of SR-AOPs induced by Fe-based catalysts [23]. And $^1O_2$ has good oxidative degradation performance to phenol-containing wastewater. According to the researches, $^1O_2$ in SR-AOPs is usually generated by oxidized superoxide radical ($O_2^{\bullet-}$) through multiple catalytic reactions, such as peroxynomosulfate (PMS) activation, Fenton reaction, photocatalysis and electrocatalytic [24]. Zhou *et al.* successfully synthesized carbon nanotube material Fe-N-C to activate PMS for phenol degradation. Fe-N-C has ample and dispersive FeN_x sites, where the electrons transfer from PMS to FeN_x site leading to $O_2^{\bullet-}$ production. And $O_2^{\bullet-}$ recombination to form large amounts of $^1O_2$, thus promoting the degradation of phenol [24]. Xu *et al.* synthesized albumin-mediated molybdenum sulfide nanocatalyst with high activity, which can activate hydrogen peroxide to generate $O_2^{\bullet-}$ and $^1O_2$. $O_2^{\bullet-}$ was mainly produced from the catalytic reaction of Mo(IV) and hydrogen peroxide, while $^1O_2$ was produced from the action of Mo(VI) and hydrogen peroxide [25]. However, previous studies have often emphasized the connection between $O_2^{\bullet-}$ and $^1O_2$, while neglecting the role of other radical can play in this pathway. The generation path of $^1O_2$ may not be limited to the above form process. $SO_4^{\bullet-}$, the most common oxide species in SR-AOPs system, does it have the potential to produce $^1O_2$? This study focused on the role of $SO_4^{\bullet-}$ in the way of $O_2^{\bullet-}$ to $^1O_2$. Further insight into the $^1O_2$ generation pathway is a significant challenge in the field of catalytic oxidation.

In this work, composite catalysts co-doped with Fe and Mo (FeMo@CNT) were prepared by introducing Fe and Mo into nitrogen-doped carbon nanotubes. BPA was chosen as object pollutant for estimating the performance of FeMo@CNT/PDS system under different conditions. The purpose of this work was to (i) study the important function of Mo to $^1O_2$ production in Fe/Mo-based SR-AOPs; (ii) reveal a new mechanism of $^1O_2$ generation from $SO_4^{\bullet-}$ and $O_2^{\bullet-}$; (iii) estimate the practical application potential of FeMo@CNT/PDS system in BPA removal.

Details of chemicals (Text S1), catalyst synthesis method (Text S2), catalyst characterization (Text S3), degradation experiments (Text S4), analytical methods (Text S5 and Table S1), electrochemical measurement (Text S6), and density functional theory (DFT) calculation (Text S7) are presented in Supporting information.

Synthesized schematic of FeMo@CNT catalyst is shown in Fig. 1a. According to the scanning electron microscope (SEM) and high-resolution transmission electron microscopy (HRTEM) pictures of Fe@CNT (Figs. 1b-d), Fe@CNT showed a bamboo-like carbon nanotube structure with a large stretching ratio. The metal particles Fe_7C_3 were wrapped in the nanotubes [26]. As shown in Figs. 1e and f, FeMo@CNT also presented a bamboo-like carbon nanotube structure. The metal particles were encapsulated inside the tubes to form a shell-nuclear structure, and the disordered accumulation between the nanotubes formed rich holes. This geometric structure was beneficial to prevent the agglomeration and dissolution of metal nanoparticles, which could effectively alleviate the metal leaching problem and increase the stabilization of materials. According to the HRTEM image of FeMo@CNT (Fig. 1g), clear lattice stripes with the particle crystal surface spacing of 0.23 nm were existed in the catalyst structure, corresponding to the (340) crystal surface of Fe_2MoC, which indicated that the metal particle was Fe_2MoC [27,28]. This finding also further successfully confirmed the synthesis of Fe/Mo-loaded carbon composite catalyst. Furthermore, according to the energy dispersive X-ray spectroscopy mapping (EDS-mapping) spectra of FeMo@CNT in Fig. 1h, the nanotubes were mainly composed of carbon and nitrogen elements, indicating that nitrogen was also successfully doped to form N-doped carbon nanotubes. The metal particles were composed of Fe and Mo elements, and the overall distribution positions of the two elements were basically the same, which revealed the successful binding of Fe and Mo.

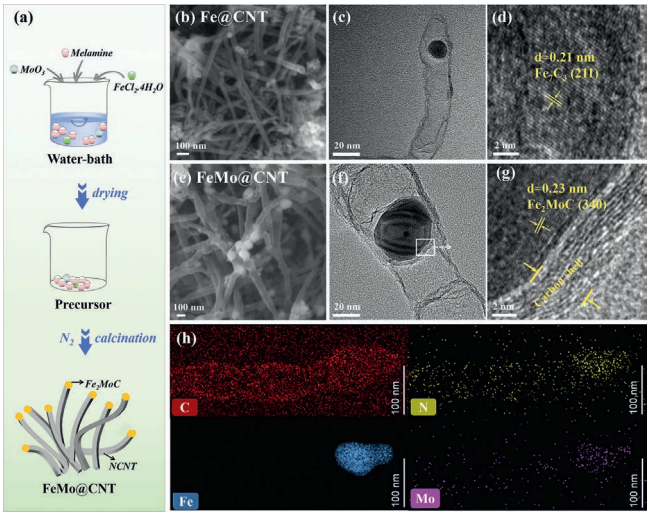


Fig. 1. (a) Synthesis image of sample FeMo@CNT. SEM and HRTEM pictures of (b-d) Fe@CNT and (e-g) FeMo@CNT. (h) TEM mapping images of FeMo@CNT.

The X-ray diffraction (XRD) showed the crystal structures of different catalyst samples (Fig. 2a). The diffractogram of Fe@CNT and Mo@CNT had characteristic peaks at 44.86° and 36.77° corresponding to the (211) lattice plane of Fe_7C_3 (PDF #17–0333) and (006) lattice plane of MoC (PDF #08–0384), respectively [29]. The composite catalyst FeMo@CNT corresponded to the (340) and (006) crystal surfaces of Fe_2MoC (PDF #17–0911), indicating that the Fe and Mo was present in the catalyst as the Fe_2MoC structure [30]. The used FeMo@CNT retained the crystal structure, showing that the catalyst equipped with good cycling stability and used catalyst still had good activity. From the X-ray photoelectron spectroscopy (XPS) spectra (Figs. 2b and c), the Fe in FeMo@CNT appeared in the form of Fe^0, Fe(II), and Fe(III) [9,31], while Mo was present in Mo(IV), Mo(V) and Mo(VI) forms [32]. Compared with Fe@CNT and Mo@CNT, the content of low-valent Fe (Fe^0, Fe(II)) and high-priced Mo (Mo(V), Mo(VI)) increased in FeMo@CNT, indicating that Mo doping promoted Fe reduction during pyrolysis. C in FeMo@CNT were mainly present in the form of C–C/C=C and C–N (Fig. S1 in Supporting information). And nitrogen source after carbonization was stored as pyrrolic N, pyridinic N, graphitic N and oxidized N. The peak of Mo-N was also detected, indicating that a small

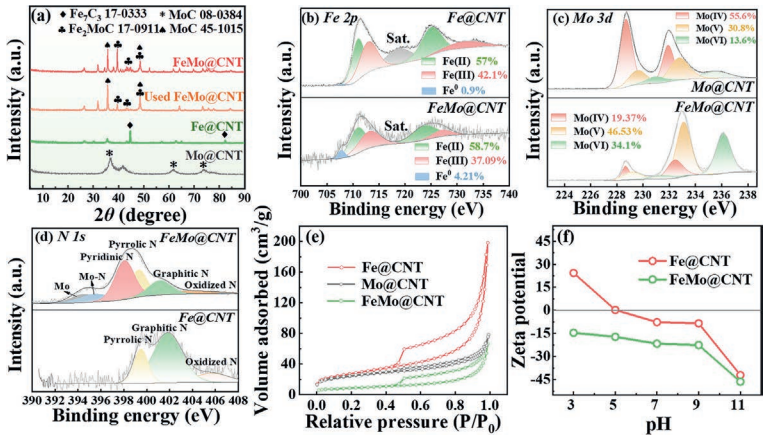


Fig. 2. (a) XRD spectra of various materials. (b) Fe 2p, (c) Mo 3d and (d) N 1s spectrogram of various materials. (e) Nitrogen adsorption/desorption curves of various materials. (f) Zeta potential of various samples in water with different initial pH.

amount of Mo was bound to the N-doped carbon network (Fig. 2d) [33,34].

Additionally, the N_2 adsorption/desorption curve (Fig. 2e, Table S2 in Supporting information) showed that specific area of FeMo@CNT was 29.87 m^2/g, which was smaller than that of Fe@CNT and Mo@CNT (95.9 m^2/g and 82.11 m^2/g). This was due to Mo introduction changing the pore dimension of monometallic material. N_2 adsorption/desorption curve of FeMo@CNT showed feature of type IV isotherm curve with a lag loop, revealing that the catalyst contained mesoporous [35]. And the pore dimension of catalyst was basically distributed between 0–70 nm (Fig. S2 in Supporting information). Moreover, FeMo@CNT had good magnetic properties (18.3 emu/g), which could be recycled by magnetic field (Fig. S3 in Supporting information) [36]. Hydrodynamic radii of various samples were shown in Table S3 (Supporting information). Fig. 2f and Table S4 (Supporting information) show the zeta potentials of both Fe@CNT and FeMo@CNT in water (pH 3–11). The absolute values of zeta potentials for FeMo@CNT were generally bigger than Fe@CNT, proving that the catalytic system after Mo introduction presented more stabilization. This facilitated the dispersion of catalyst in solution and heightened catalytic activity [37].

BPA degradation and adsorption in various systems are exhibited in Figs. 3a and b and Fig. S4 (Supporting information). Compared with Fe@CNT/PDS and Mo@CNT/PDS system, BPA degradation in FeMo@CNT/PDS (Fe:Mo = 1:1) system had been greatly improved. Within 30 min, FeMo@CNT/PDS system could remove BPA rapidly and completely. However, the degradation efficiency of Fe@CNT/PDS and Mo@CNT/PDS systems for BPA were only 60 % and 51 %, respectively. This suggested that the synergistic benefits of Fe and Mo improved the degradation capacity of catalytic system. Moreover, the optimal Mo doping amount was also explored (Figs. 3c and d and Fig. S5 in Supporting information). With the rise of Mo content, removal rate of BPA evidently increased to a peak and subsequently decreased. When the Fe/Mo molar ratio was 1:1, BPA could be completely degraded within 30 min and the k_{obs} reached the highest value (0.444 min^{-1}). Therefore, Fe_1Mo_1@CNT (FeMo@CNT) was selected as the optimal catalyzer. Comparison of FeMo@CNT/PDS system with some other oxidation systems were shown in Fig. 3e and Table. S5 (Supporting information) [38–44]. The data indicated that BPA degradation performance under FeMo@CNT/PDS system was more superior than various systems based on SR-AOPs significantly. This demonstrated outstanding BPA degradation performance of this system.

The effect of pH on FeMo@CNT/PDS system are shown in Figs. 3f and g and Fig. S6 (Supporting information). At wide pH conditions (pH 3–9), BPA could be completely degraded, and the more acidic the solution, the more favorable the decomposition of BPA was. However, the degradation was significantly inhibited at pH 11, probably attributed to that Fe(II) was more likely to bind with OH^- at strong alkaline environment, which inhibited PDS activation [45]. The k_{obs} of BPA degradation was significantly larger than adsorption at various pH value, indicating that FeMo@CNT/PDS system had good PDS activation performance. In contrast, the Fe@CNT/PDS system showed a poor PDS activation performance under various pH values (Fig. S7 in Supporting information). This revealed that inducted Mo promoted the PDS activation of catalytic system. BPA degradation under complex environmental substrates (inorganic anions and HA) was still able to reach 100 % in Fe/Mo@CNT/PDS system (Fig. 3h). The date revealed that this system had superior interference resistance to environmental substrates. ICP test was conducted after FeMo@CNT was used in the batch experiment and the leaching concentrations of Fe and Mo ions were 0.03 and 0.08 mg/L, respectively (Fig. S8 in Supporting information). The content of Fe and Mo ions was maintained at low concentration, which showed a weak influence on the degradation of BPA (Fig. S9 in Supporting information) [46]. The above results showed great practical application potential for Fe/Mo@CNT/PDS system.

The FeMo@CNT/PDS system also exhibited high degradation capability for other organic contaminants (Fig. 4a and Fig. S10 in Supporting information). Objective contaminants containing BPA, PE, 4-CP, HBAC, SA and *p*-NP were chosen to assess the oxidation capability of Fe@CNT/PDS and FeMo@CNT/PDS system. Low adsorption capabilities were presented to both Fe@CNT and FeMo@CNT for various pollutants removal. However, after adding PDS, the catalysts could decompose different pollutants quickly. The degradation efficiencies of BPA, 4-CP, PE, SA, HBAC, BA and *p*-NP under FeMo@CNT/PDS system were 100 %, 98.3 %, 97.2 %, 77.3 %, 67.1 %, 66.2 % and 20 %, respectively, which were significantly bigger than Fe@CNT system. Comparing the degradation k_{obs} to different organics in Fe@CNT/PDS and FeMo@CNT/PDS system further showed that Mo doping into the Fe-based catalyst significantly promoted the PDS activation and thus improved the degradation performance of pollutants. These results effectively manifested the significance of Mo in enhancing catalytic oxidation capacity.

Different organics showed different degradation efficiencies in the FeMo@CNT/PDS system, so we further explored the fundamental of the selective removal for different organics by this system. The redox potential of organics could be identified by cyclic voltammetry (CV). And half-wave potential ($\varphi_{1/2}$) of various organics could represent their redox potential [47]. Among the selected contaminants, there was lowest $\varphi_{1/2}$ value (0.442 V) for BPA, which

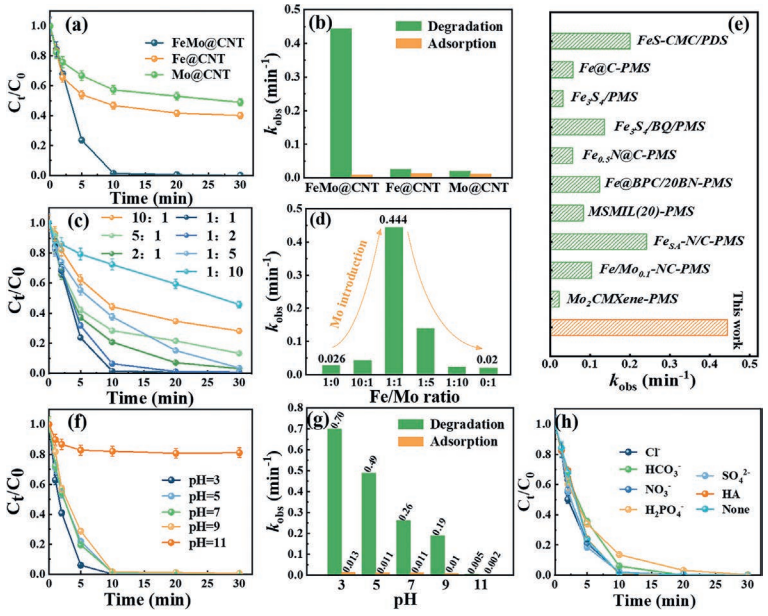


Fig. 3. (a) Degradation and (b) degradation/adsorption k_{obs} of BPA under various catalytic systems. (c) Degradation and (d) degradation/adsorption k_{obs} of BPA in catalysts with various Fe/Mo ratios. (e) Comparison of degradation k_{obs} in various oxidation systems for BPA removal. (f) Degradation and (g) degradation/adsorption k_{obs} of BPA in FeMo@CNT/PDS systems with different initial pH. (h) BPA degradation in FeMo@CNT/PDS system under various water substrates. Experimental parameters: [HA] = 10 mg/L, [Cl^-] = 50 mg/L, [SO_4^{2-}] = 50 mg/L, [HCO_3^-] = 20 mg/L, [NO_3^-] = 20 mg/L, [$H_2PO_4^-$] = 20 mg/L.

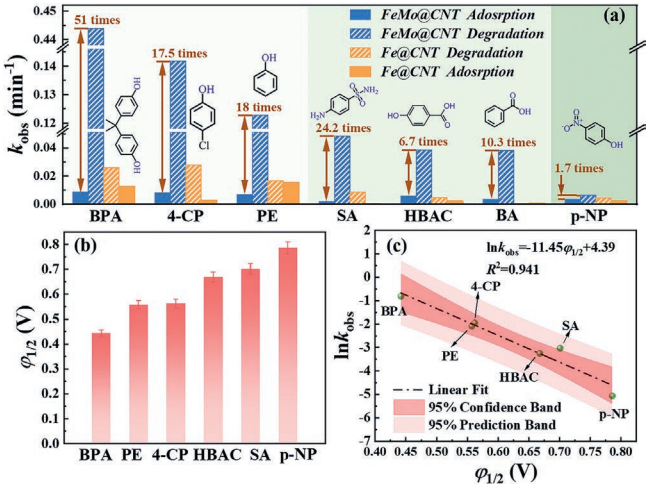


Fig. 4. (a) The degradation/adsorption k_{obs} values for various organics in various systems. Catalyst content: 0.1 g/L, PDS content: 0.4 g/L, organic concentrations: 0.1 mmol/L. (b) Obtained $\varphi_{1/2}$ values of various organics. (c) The correlation between $\varphi_{1/2}$ values of organics and their k_{obs}.

was followed by PE < 4-CP < HBAC < SA < *p*-NP (Fig. 4b). Fig. 4c revealed the correlation between $\varphi_{1/2}$ values of various organics and their degradation k_{obs} values under FeMo@CNT/PDS system. Obviously, the $\varphi_{1/2}$ values of organics (BPA, 4-CP, SA, HBAC, PE, and *p*-NP) were significant correlations with their lnk_{obs} values. The date revealed that selective removal of organics by FeMo@CNT/PDS system was strongly relevant with the redox potential. Briefly, the higher redox potential of an organic pollutant the more difficult it is to be degraded in FeMo@CNT/PDS system.

ROS quenching tests were carried out to identify main species of ROS produced in FeMo@CNT/PDS system. EtOH was utilized as scavenger for $^{\bullet}OH$ (1.9×10^9 L mol^{-1} s^{-1}) and $SO_4^{\bullet-}$ (4.3×10^7 L mol^{-1} s^{-1}) [48]. TBA, FFA and *p*-BQ were used as $^{\bullet}OH$, $^1O_2$ and $O_2^{\bullet-}$ quenchers to evaluate their contribution for BPA removal ($k_{TBA\text{-}^{\bullet}OH} = 5.2 \times 10^8$ L mol^{-1} s^{-1}, $k_{FFA\text{-}^1O_2} = 1.2 \times 10^8$ L mol^{-1} s^{-1}, $k_{p\text{-}BQ\text{-}O_2^{\bullet-}} = 1 \times 10^9$ L mol^{-1} s^{-1}) [49–51]. As exhibited in Fig. 5a and Fig. S11 (Supporting information), BPA removal rate was reduced from 100 % without quencher to 43 %, 22.1 % and 5.4 % with EtOH, FFA and *p*-BQ, respectively. And the k_{obs} of BPA degradation were 0.045 min^{-1} (with 200 mmol/L EtOH), 0.02 min^{-1} (with 100 mmol/L FFA) and 0.007 min^{-1} (with 25 mmol/L *p*-BQ), which were much smaller than 0.44 (without scavenger), suggesting that $^1O_2$, $O_2^{\bullet-}$ and $SO_4^{\bullet-}$ might be the main ROS (Fig. 5b). Additionally, the introduction of TBA had slight impact on the degradation of BPA. These implied that $^1O_2$, $O_2^{\bullet-}$ and $SO_4^{\bullet-}$ were prominent in the FeMo@CNT/PDS system, while the $^{\bullet}OH$ was almost inexistent. And the accelerated degradation effect of BPA in D_2O as the solvent further proved the presence of $^1O_2$ (Fig. S12 in Supporting information). D_2O could been used to test $^1O_2$ because the life span of $^1O_2$ in D_2O was far longer than that H_2O [52].

Electron paramagnetic resonance (EPR) tests were illustrated in Figs. 5c and d. The test data were basically consistent with radical quenching experiment. Signals of TEMP-$^1O_2$ and DMPO-$SO_4^{\bullet-}$ in FeMo@CNT/PDS system were clearly observed and more obvious than Fe@CNT/PDS system. This suggested a stronger oxidizing capacity of the FeMo@CNT/PDS system than Fe@CNT/PDS system through the production of more reactive species, which was agreed with the date of above quenching tests [53]. This further affirmed the significant function of $SO_4^{\bullet-}$ and $^1O_2$ in BPA removal. The results also displayed the pivotal role of Mo introduction which observably facilitated ROS production in Fe-based SR-AOPs [54].

According to the above, $^1O_2$, $O_2^{\bullet-}$ and $SO_4^{\bullet-}$ dominated the occurrence of reaction system. There may be some transforming relationship between these ROS. We introduced different sacrificial agents in FeMo@CNT/PDS system to monitor the content variation of $^1O_2$ (Fig. 5e). The peak intensity of TEMP-$^1O_2$ was substantially diminished after introducing a small amount of EtOH (the quencher for $^{\bullet}OH$ and $SO_4^{\bullet-}$) or *p*-BQ (quencher for $O_2^{\bullet-}$). The peak intensity was disappeared in the system with 100 mmol/L EtOH or 25 mmol/L *p*-BQ. These suggested that $SO_4^{\bullet-}$ and $O_2^{\bullet-}$ influenced the production of $^1O_2$, while $^{\bullet}OH$ proved absent in the radical quenching experiments [53]. In addition, EPR test was used to monitor the concentration of $O_2^{\bullet-}$ at different reaction times to demonstrate $O_2^{\bullet-}$ generation and intermediate conversion (Fig. S13 in Supporting information). According to the experimental data,

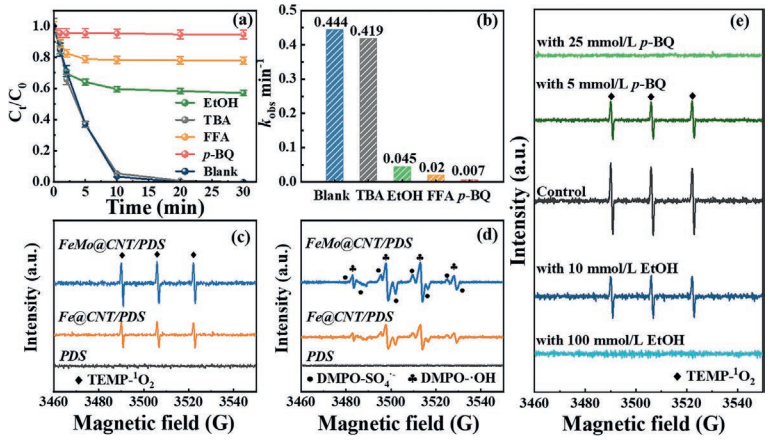


Fig. 5. (a) BPA degradation effect and (b) k_{obs} with different quenchers under FeMo@CNT/PDS system. EPR spectrum of (c) TEMP and (d) DMPO under various systems. (e) EPR spectra of TEMP-$^1O_2$ obtained at 10 min with the presence of EtOH and *p*-BQ. Experimental parameters: [BPA] = 20 mg/L, [EtOH] = 200 mmol/L, [FFA] = 100 mmol/L, [TBA] = 50 mmol/L, [*p*-BQ] = 25 mmol/L.

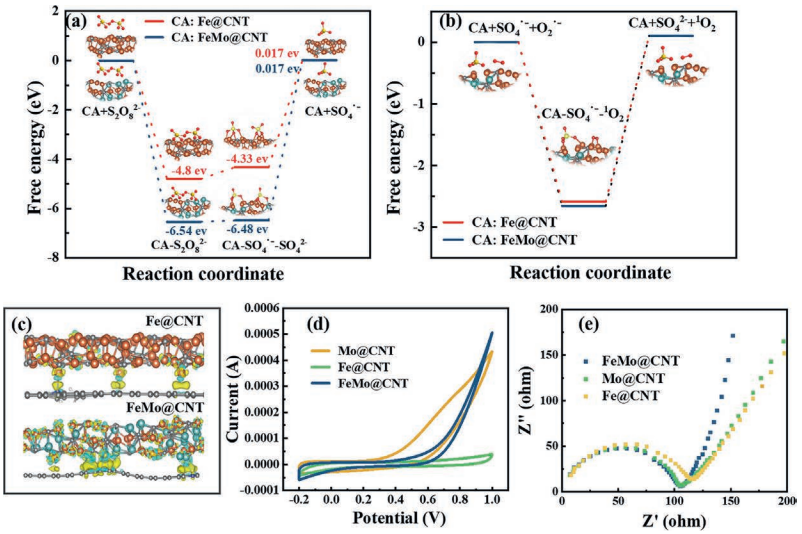


Fig. 6. (a) Reaction paths of PDS activation and (b) $^1O_2$ production at Fe sites under different systems. (c) Differential charge density in various catalysts. (d) Cyclic voltammograms of various samples. (e) The electrochemical impedance spectrum of various samples.

the content of $O_2^{\bullet-}$ increased first and then decreased gradually with the reaction. This further confirmed the generation and transformation of $O_2^{\bullet-}$. Based on the above results, $O_2^{\bullet-}$ might be oxidized into $^1O_2$ by $SO_4^{\bullet-}$ in FeMo@CNT/PDS system.

Aforementioned experimental data suggested that $O_2^{\bullet-}$ and $SO_4^{\bullet-}$ exhibited a pivotal role to $^1O_2$ generation during catalytic oxidation by FeMo@CNT/PDS system, but specific production principle was still not clear. Therefore, the $^1O_2$ production with $O_2^{\bullet-}$ and $SO_4^{\bullet-}$ conversion was further researched by DFT calculations [55]. Optimized models (FeMo@CNT and Fe@CNT) were established based on molecular structures of materials (Fig. S14 in Supporting information). As presented in Fig. 6a, the energy barrier of PDS adsorption onto FeMo@CNT was figured out as −6.54 eV smaller than Fe@CNT (−4.8 eV), showing that Mo introduction facilitated the capture of PDS for succedent activation. In FeMo@CNT/PDS system, the bond length of O–O (l_{O5-O6}) raised from 4.73 Å to 5.07 Å after Mo introduction, suggested that O–O bonds were more easier to fracture [56]. The bond angle between O-S-O was spread to 107.15° and l_{O5-O6} further extended for $SO_4^{\bullet-}$ desorption during further activation. This process had the energy barrier of −6.48 eV and was accompanied by heat absorption. While in Fe@CNT/PDS system, total energy barrier for PDS activation was −4.33 eV, revealing that introduced Mo could facilitate O–O cleavage and PDS activation [57]. Fig. 6b reveals the generation mechanism of $^1O_2$ converted from $O_2^{\bullet-}$ and $SO_4^{\bullet-}$ where $O_2^{\bullet-}$and $SO_4^{\bullet-}$ bound undergo redox reactions to generate $^1O_2$ on the surface of catalyst. Subsequently the generated $^1O_2$ and $SO_4^{\bullet-}$ of adsorbed state will be released from the catalyst surface (Eq. 1 and Fig. S15 in Supporting information). By comparing the reaction energy barrier of different systems, the formation energy barrier of $^1O_2$ in FeMo@CNT/PDS system was 2.69 eV, slightly lower than Fe@CNT/PDS system (2.76 eV) [58]. This result confirmed that doped Mo facilitated $^1O_2$ production in the FeMo@CNT/PDS system.

$$O_2^{\bullet-} + SO_4^{\bullet-} \rightarrow {}^1O_2 + SO_4^{2-} \quad (1)$$

In addition, we explored the main active sites of samples by differential charge density (Fig. 6c). The results showed that charge transfer distributed basically in Fe-C/N site, where electron transferred from Fe to C/N. Charge accumulation was more significant in FeMo@CNT compared to Fe@CNT, showing that charge transfer of catalytic system was promoted by doped Mo. Cyclic voltammetry tests further showed the process of catalytic oxidation by FeMo@CNT. Compared to Fe@CNT/PDS and Mo@CNT/PDS system, oxidizing potential of FeMo@CNT/PDS system turned to a higher value (Fig. 6d). This manifested that Mo doping promoted the redox reaction on the catalyst surface, which enabled

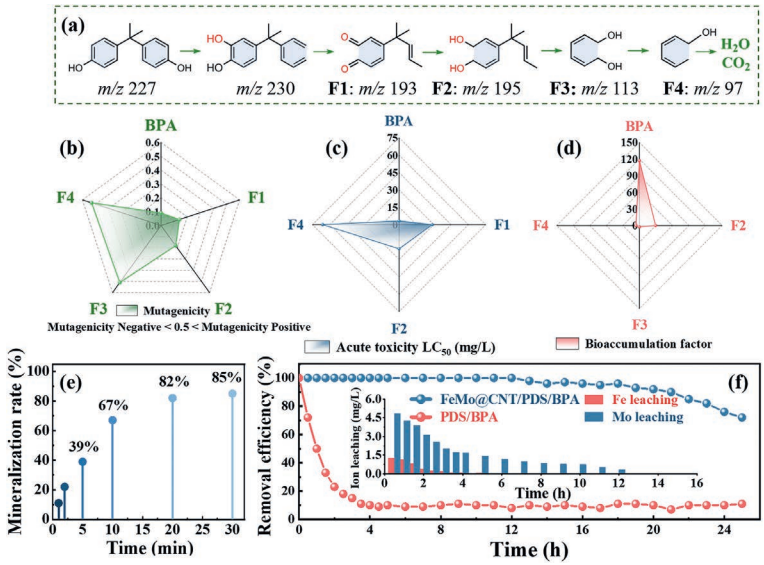


Fig. 7. (a) BPA removal pathways under FeMo@CNT/PDS system. (b) Mutagenicity, (c) acute toxicity LC_{50} and (d) bioaccumulation factor of BPA and intermediates. (e) The mineralization rate of BPA degradation under FeMo@CNT/PDS system. (f) BPA degradation in a microreactor. Experiment parameters: BPA content: 20 mg/L, PDS content: 0.4 g/L, attempt time = 25 h, flow rate = 25 mL/min.

FeMo@CNT to activate PDS efficiently [55]. Further, electrochemical impedance spectrum was exhibited in Fig. 6e. Radius of FeMo@CNT was smaller than Fe@CNT and Mo@CNT, demonstrating that charge transfer resistance of Fe@CNT was decreased after Mo introduction, which quickened the electron transfer to promote activation capacity of catalyst. According to the above results, Mo helped promote the charge transfer efficiency of catalyst and accelerate PDS decomposition, which boosted the production of $SO_4^{\bullet-}$ and $^1O_2$ from $O_2^{\bullet-}$ oxidized by $SO_4^{\bullet-}$ and further improved the degradation performance of pollutants.

HPLC-MS analysis in full scan mode was used to provide comprehensive analysis of BPA degradation path under FeMo@CNT/PDS system. These were based on intermediate products of BPA degradation, including the destruction reaction and hydroxylation reaction of the benzene ring (Fig. 7a) [59]. First, **F1** was formed after hydroxylation, ring-cleavage reaction and ketylation reaction of BPA parent. Subsequently, **F2** was generated by the hydrogenation reaction, and with further breaking of the carbon chain, **F2** can be converted into **F3** and **F4**. And finally, **F4** could be decomposed and converted into H_2O and CO_2. BPA was degraded more quickly and thoroughly in FeMo@CNT/PDS system compared to Fe@CNT/PDS system (Fig. S16 in Supporting information). Besides, the intermediates degraded ineffectively under Fe@CNT/PDS system ($m/z = 230$) could be further decomposed under FeMo@CNT/PDS system. The signal peaks of MS-ESI scans were low under Fe@CNT/PDS system, which might attribute to weak oxidizing capability. Compared with degradation paths of other catalyst systems that have been reported, BPA removal path under FeMo@CNT/PDS system was simpler and more efficient. These explained the significance of doped Mo to rapid and efficient removal of BPA.

Toxicity Estimation Software Tool (T.E.S.T.) was utilized to forecast toxicity of above degradation products (Text S8 in Supporting information). Mutagenicity of intermediates was decreasing with oxidation reaction and ultimately converted to mutagenicity positive (Fig. 7b). Intermediates **F1** and **F2** were mutagenicity negative, while products **F3** and **F4** were mutagenicity positive. And LC_{50} toxicity of intermediates declined evidently with reaction proceeded (Fig. 7c). Fig. 7d revealed the bioaccumulation factor of products. As expected, bioaccumulation factors of reaction products decreased to harmless remarkably under FeMo@CNT/PDS system [60]. Biological toxicity assays (using *V. qinghaiensis* Q67 luminescent bacteria) were performed to empirically demonstrate altered toxicity in FeMo@CN/PDS/BPA system (Fig. S17 in Supporting information). The inhibition rate of luminescent bacteria was 16.6 % at 30 min, which was reduced by 44.8 % compared with the original BPA. This showed excellent detoxification ability for BPA containing pollutants. In addition, we monitored the degree of mineralization of the system. After 30 min, the mineralization rate was 85 %, showing good BPA purification ability of catalytic system (Fig. 7e and Text S9 in Supporting information).

The dynamic catalytic capability and long stabilization of material was evaluated using a microreactor filling FeMo@CNT-loaded polyurethane (PU) sponges (Text S10 in Supporting information). Photograph and schematic diagram of assembled reactor are presented in Figs. S18 and S19 (Supporting information), where ten pieces of FeMo@CNT-loaded PU sponges were filled in reactor. Experimental data revealed that BPA could still be completely degraded after 12 h of continuous dynamic degradation in FeMo@CNT-loaded microreactor (Fig. 7f). And BPA removal efficiency remained above 80 % after 23 h of continuous dynamic degradation. These showed excellent catalytic activation properties and stability of FeMo@CNT. In contrast, microreactor that do not load FeMoCNT had poor degradation performance. Additionally, the ionic leaching was also detected during the dynamic degradation process. Initially, a small amount of Fe and Mo ions were lost in solution, and as reaction proceeded, the ion overflow content gradually decreased and eventually disappeared, displaying good practical utilization potential.

Composite material (FeMo@CNT) was prepared *via* introducing Fe and Mo into N-doped carbon nanotubes and utilized to degrade BPA by PDS activation. Compared with single-metal catalysts, the catalytic activity of FeMo@CNT/PDS system was significantly improved. FeMo@CNT/PDS system can completely degrade BPA within 30 min and had a high degradation rate in the presence of wide pH and various environmental substrates. The enhanced catalytic activity of FeMo@CNT was mainly attributed to Mo doping. Mo can improve the electron transfer efficiency on catalyst surface, accelerate PDS decomposition and promote ROS generation. The experimental results showed that this system was dominated by $SO_4^{\bullet-}$ and $^1O_2$. We further revealed the mechanism of $^1O_2$ generation derived from $O_2^{\bullet-}$ oxidized by $SO_4^{\bullet-}$. Furthermore, Mo introduc-

tion into FeMo@CNT could effectively promote PDS activation and reduce energy barrier of $^1O_2$ production, thus realizing the improvement of both $SO_4^{\bullet-}$ and $^1O_2$. After catalytic oxidation reaction, the overall toxicity was decreased significantly. And the continuous degradation of BPA with the reactor loaded with FeMo@CNT in dynamic experiments also further demonstrated the stability and practical potential of FeMo@CNT/PDS system. This work offers new ideas for establishing efficient catalytic systems and enriches the theoretical research of AOPs introduced by radical and non-radicals.

However, there are still some limitations for this study: (i) Real wastewater and environmental matrix are often more complex and different from simulated wastewater; (ii) although Fe/Mo@CNT have excellent catalytic activity and stability, the release of metal ions cannot be completely avoided. Future research can be combined with other advanced processing technologies such as photocatalysis and electrocatalysis to improve the catalytic performance for persulfate activation. The successful experimental theories and models can be used to solve practical environmental problems. And nanoconfined catalysts can be constructed to further avoid the leaching of metal ions.

CRediT authorship contribution statement

Taozhen Li: Writing – original draft, Methodology, Investigation, Formal analysis, Conceptualization. **Zhuohang Wu:** Formal analysis, Data curation. **Shu Yang:** Writing – review & editing, Supervision, Software. **Bin Li:** Validation, Formal analysis. **Semencha Alexander Vyacheslavovich:** Writing – review & editing. **Donaev Sardor Burkhanovich:** Writing – review & editing. **Ergashev Yorqinjon Tolqinogli:** Writing – review & editing. **Rashidov Shokhzodbek Abduvakhobovich:** Writing – review & editing. **Lei Wang:** Writing – review & editing, Supervision. **Jingwen Pan:** Writing – review & editing, Supervision, Project administration, Conceptualization.

Declaration of competing interest

The authors declare that they have no known competing financial interests or personal relationships that could have appeared to influence the work reported in this paper.

Acknowledgments

This work was supported by the National Natural Science Foundation of China (Nos. 52272222, 52300207, and 52204423), Natural Science Foundation of Shandong Province (No. ZR2023QE211), and Taishan Scholar Foundation of Shandong Province (No. tstp20250729). The authors also thank Fan Li (from Scientific Compass www.shiyanjia.com) for the DFT calculation.

Supplementary materials

Supplementary material associated with this article can be found, in the online version, at doi:10.1016/j.cclet.2026.112443.

References

[1] C. Yu, C. Yan, J. Gu, et al., J. Clean. Prod. 427 (2023) 139334.
[2] J. Gao, R.F. Nunes, K. O'Shea, et al., Water Res. 219 (2022) 118457.
[3] T. Peng, H. Zhang, S. Xia, et al., ACS EST Water 3 (2022) 213–226.
[4] F. Lu, T. Lin, H. Chen, Water Res. 248 (2024) 120887.
[5] J. Wang, H. Wang, L. Shen, et al., Water Res. 244 (2023) 120530.
[6] Y. Long, Z. Cao, W. Wu, et al., App. Catal. B: Environ. 344 (2023) 123643.
[7] Y.-D. Dong, Y. Shi, Y.-L. He, et al., Ind. Eng. Chem. Res. 62 (2023) 10828–10848.
[8] W. Liu, P. Fu, Y. Zhang, et al., Proc. Natl. Acad. Sci. U. S. A. 120 (2023) e2218813120.
[9] Y. Sun, C. Ma, D. Wu, et al., Water Res. 244 (2023) 120542.
[10] M. Zhong, M. Li, Q. Zhang, et al., J. Clean. Prod. 382 (2023) 135219.
[11] C. Dong, Y. Bao, T. Sheng, et al., App. Catal. B: Environ. 286 (2021) 119930.
[12] C. Dong, J. Ji, B. Shen, et al., Environ. Sci. Technol. 52 (2018) 11297–11308.
[13] J.L. Fiorio, M.A.S. Garcia, M.L. Gothe, et al., Coord. Chem. Rev. 481 (2023) 215053.
[14] Z. Zhao, B. Kang, J. Xu, et al., Carbon 209 (2023) 117995.
[15] X. Mou, J. Ma, S. Zheng, et al., Adv. Funct. Mater. 31 (2020) 2006076.
[16] C. Zhong, S. Zhang, S. Yang, et al., Chem. Eng. J. 466 (2023) 143298.
[17] J. Ye, J. Dai, D. Yang, et al., J. Hazard. Mater. 421 (2022) 126715.
[18] L.Z. Huang, C. Zhou, M. Shen, et al., J. Hazard. Mater. 389 (2020) 122137.
[19] Y. Yang, W. Ren, K. Hu, et al., Chem. Catal. 2 (2022) 1858–1869.
[20] K.H.H. Aziz, F.S. Mustafa, M.A.H. Karima, et al., Mater. Adv. 6 (2025) 3433.
[21] Y. Yan, Z. Wei, X. Duan, et al., Environ. Sci. Technol. 57 (2023) 12153–12179.
[22] Y. Zhao, L. Yu, C. Song, et al., Environ. Sci. Technol. 56 (2022) 10710–10720.
[23] M. Wang, F. Wang, P. Wang, et al., Sep. Purif. Technol. 326 (2023) 124806.
[24] J. He, Y. Wan, W. Zhou, J. Hazard. Mater. 405 (2021) 124199.
[25] Y. Xu, W. Yang, Y. Han, et al., Small. 19 (2023) 2207544.
[26] M. Zhang, J. Ren, Y. Yu, Mol. Catal. 505 (2021) 111506.
[27] X. Hao, J. Bi, W. Wang, et al., J. Power. Sources. 451 (2020) 227802.
[28] Y. Ma, K. Du, Y. Guo, et al., Chem. Eng. J. 431 (2022) 134065.
[29] J. Liu, Y. Guo, X.-Z. Fu, et al., Green Energy Environ. 8 (2023) 459–469.
[30] Z. Yan, M. Zhang, J. Xie, et al., App. Catal. B: Environ. 165 (2015) 636–641.
[31] H. Wang, C. Tang, L. Wang, et al., App. Catal. B: Environ. 333 (2023) 122755.
[32] Q. Liu, Q. Su, W. Cheng, et al., App. Catal. B: Environ. 340 (2024) 123188.
[33] J. Balamurugan, P.M. Austeria, J.B. Kim, et al., Adv. Mater. 35 (2023) 2302625.
[34] Y.X. Huang, L.Q. Yu, K.Y. Chen, et al., Chin. Chem. Lett. 35 (2024) 109437.
[35] S. Gao, Z. Wang, L. Ma, et al., ACS Catal. 10 (2019) 1375–1380.
[36] M.A.H. Karim, K.H.H. Aziz, J. Water Process. Eng. 75 (2025) 108014.
[37] Y. Jiang, R. Raliya, J.D. Fortner, et al., Environ. Sci. Technol. 50 (2016) 6964–6973.
[38] X. Liu, P. Shao, S. Gao, et al., Water Res. 226 (2022) 119218.
[39] Z. Tan, J. Tan, Z. Yang, et al., Chemosphere 335 (2023) 139129.
[40] W. Chen, L. Lei, K. Zhu, et al., J. Environ. Sci. 129 (2023) 213–228.
[41] T. Yang, S. Fan, Y. Li, et al., Chem. Eng. J. 419 (2021) 129590.
[42] X. Chen, F.O. Gudda, X. Hu, et al., NPJ Clean. Water 5 (2022) 66.
[43] D. Roy, S. Neogi, S. De, Chem. Eng. J. 428 (2022) 131028.
[44] Y. Wan, W. Zhang, X. Han, et al., J. Hazard. Mater. 430 (2022) 127832.
[45] J. Fan, J. Liu, Y. Cai, et al., Chem. Eng. J. 466 (2023) 143168.
[46] K.O. Rahman, K.H.H. Aziz, J. Environ. Chem. Eng. 10 (2022) 109015.
[47] K. Yin, Y. Shang, D. Chen, et al., App. Catal. B: Environ. 338 (2023) 123029.
[48] F.S. Mustafa, K.H.H. Aziz, Process Saf. Environ. 170 (2023) 436.
[49] C. Zhu, F. Zhu, D.D. Dionysiou, et al., Water Res. 139 (2018) 66–73.
[50] C. Tan, H. Wu, H. He, et al., Water Res. 185 (2020) 116252.
[51] L. Gao, Y. Guo, J. Zhan, et al., Water Res. 221 (2022) 118730.
[52] Y.Y.Y. Lei, X. Lei, X. Liang, et al., Environ. Sci. Technol. 50 (2023) 5433–5444.
[53] Y. Huang, S. Zhao, K. Chen, et al., Front. Environ. Sci. Eng. 18 (2024) 134.
[54] B. Shao, H. Dong, B. Sun, et al., Environ. Sci. Technol. 53 (2018) 894–902.
[55] B. Hou, J. Pan, T. Shi, et al., J. Hazard. Mater. 464 (2024) 133020.
[56] J. Pan, B. Gao, P. Duan, et al., J. Mater. Chem A 9 (2021) 11604–11613.
[57] Y. Wang, X. Li, M. Zhang, et al., Adv. Mater. 32 (2020) e2000231.
[58] M. Wu, S. Tang, Z. Wang, et al., Chin. Chem. Lett. 36 (2025) 110613.
[59] X. Zhang, X. Wang, R. Zhu, et al., J. Environ. Manag. 328 (2023) 116894.
[60] T. Li, J. Pan, X. Wang, et al., Chem. Eng. J. 477 (2023) 147000.